Revision

17th September 2015

Intrinsically Microporous Polymer Retains Porosity in Vacuum Thermolysis to Electroactive Heterocarbon

---

Yuanyang Rong [1], Daping He [1], Adrian Sanchez-Fernandez [1], Craig Evans [1], Karen J. Edler [1], Richard Malpass-Evans [2], Mariolino Carta [2], Neil B. McKeown [2], Tomos J. Clarke [3], Stuart H. Taylor [3], Andrew J. Wain [4], John M. Mitchels [1], and Frank Marken *[1]

[1] Department of Chemistry, University of Bath, Claverton Down, Bath BA2 7AY, UK
[2] School of Chemistry, University of Edinburgh, West Mains Road, Edinburgh, EH9 3JJ, UK
[3] School of Chemistry, Cardiff University, Main Building, Park Place, Cardiff CF10 3AT, UK
[4] National Physical Laboratory, Teddington, United Kingdom, TW11 0LW, UK

To be submitted to Langmuir

Proofs to F. Marken (f.marken@bath.ac.uk)

Abstract

Vacuum carbonisation of organic precursors usually causes considerable structural damage and collapse of morphological features. However, for a polymer with intrinsic microporosity (PIM-EA-TB with a BET surface area of 1027 m^2g^{-1}) it is shown here that the rigidity of the molecular backbone is retained even during 500 °C vacuum carbonisation yielding a novel type of microporous hetero-carbon (either as powder or as thin film membrane) with properties between those of a conducting polymer and those of a carbon. After carbonisation, the SEM morphology and the SAXS Guinier radius remain largely unchanged as does the cumulative pore volume. However, the BET surface area is decreased to 242 m^2g^{-1}, but microporosity is considerably increased. The new material is shown to exhibit noticeable electrochemical features including two pH-dependent capacitance domains switching from ca. 33 Fg^{-1} (when oxidised) to ca. 147 Fg^{-1} (when reduced), a low electron transfer reactivity towards oxygen and hydrogen peroxide, and a four-point-probe resistivity (dry) of approximately 40 MΩ/square for a 1-2 μm thick film.

Keywords: supercapacitor, electrocatalysis, peroxide, oxygen, fuel cell, membrane, sensing.

Graphical Abstract:

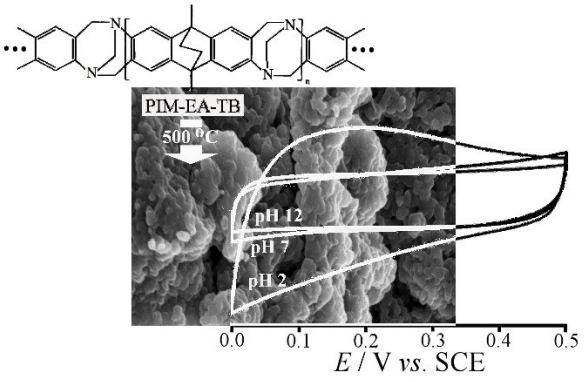

1. Introduction

Vacuum carbonisation[1,2] offers a direct approach to the formation of porous carbon products[3,4,5] via conversion of organic precursor materials such as cellulose,[6,7] starches,[8,9] chitosan,[10,11] poly-acrylonitrile,[12,13] poly-pyridine,[14] graphene oxide,[15,16] or other types of carbon sources.[17,18] Charring may occur under mild conditions, but graphitisation only takes place at much higher temperatures (beyond 1000 ^{o}C) yielding more ordered and more electrically conducting forms of carbon.[19,20] In this case a clear link between the precursor molecular structure and the carbonised product structure is not usually evident due to complex fragmentation and backbone cross-linking processes occurring in such organic materials. Hence, controlling the physical and chemical properties of carbons produced in this way can be highly challenging. Synthesis methods for mesoporous carbons have been introduced based on clay additives controlling pore size.[21] Mild carbonisation without significant morphology changes has been reported recently for ZIF-8 type materials[22,23] and for rigid porous metal-organic framework materials,[24,25] with applications for example in CO_2 capture[26] and in battery systems.[27] Therefore, a highly rigid precursor material can be advantageous. Here, a highly rigid and thermally robust polymer of intrinsic microporosity (PIM) is employed to demonstrate the case of mild carbonisation without structural collapse and, uniquely, without loss of backbone nitrogen functionalities. The remaining nitrogen functionality is associated with a proton-transfer associated step in capacitance.

PIM materials[28] have been developed for applications in gas separation[29,30,31] and for gas sensing.[32] Recently, structures such as PIM-EA-TB (see Figure 1) have been shown to also provide novel properties for applications in electrocatalysis[33] or for electrochemically active membranes. The presence of protonation sites (two tertiary nitrogen functionalities in PIM-EA-TB, see Figure 1) affect ion conductivity and "ionic diode" phenomena.[34] It is shown here that these structural nitrogen atoms as well as intrinsic porosity are retained during mild carbonisation with interesting effects on the properties of the resulting pH-switchable supercapacitive microporous hetero-carbon.

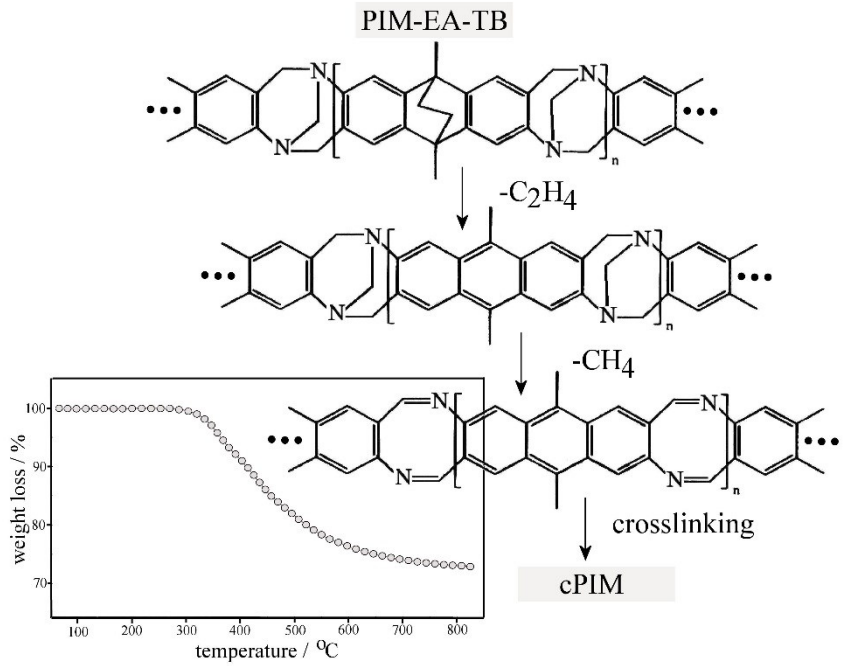

Figure 1. Molecular structure of PIM-EA-TB and hypothetical scheme for thermolysis processes indicating ethylene and methane loss (corresponding to *ca*. 15% weight loss). Also shown in the thermogravimetric trace for PIM-EA-TB under nitrogen with *ca*. 18% weight loss at 500 ºC.

In this report it is demonstrated that 500 ºC vacuum carbonisation of PIM-EA-TB precursor results in the formation of a novel hetero-carbon material with (i) high microporosity, (ii) low electrical conductivity, (iii) a high pH-switchable capacitance with two distinct proton concentration dependent potential domains, (iv) low electron transfer reactivity towards oxygen and hydrogen peroxide, and (v) retention of morphology (as powder or film) during carbonisation.

2. Experimental

2.1. Chemical Reagents

Chloroform, phosphoric acid (85%) and sodium hydroxide were purchased from Aldrich and used without further purification. PIM-EA-TB was obtained following a literature recipe.[35] Solutions were prepared with filtered and deionized water of resistivity of 18.2 MΩ cm from a Thermo Scientific water purification system (ELGA).

2.2. Instrumentation

A potentiostat system (IVIUM Compactstat) was employed with a Pt wire counter electrode and a KCl-saturated calomel reference (SCE, Radiometer, Copenhagen). The working electrode was prepared from ITO coated glass (tin-doped indium oxide film sputter-coated onto glass, active area 10 mm × 10 mm, resistivity ca.15 Ω / square) obtained from Image Optics Components Ltd (Basildon, Essec, UK). SECM measurements were performed using 10 μm diameter Pt SECM probe controlled by a CHI 900B system (CH Instruments, Texas). Generator-collector experiments were undertaken by biasing the tip

at a fixed potential of 0.6 V (sufficient to oxidise H_2O_2) whilst sweeping the substrate potential at a tip-surface separation of approximately 5 μm.

Four-point probe measurements were performed with a film on a glass slide using a Jandel system. Electron micrographs were obtained on a field emission scanning electron microscope (JEOL FESEM6301F). Raman spectroscopy studies were carried out with a Renishaw Raman microscope system with a resolution of about 2 cm^{-1} and using an excitation wavelength of 532 nm. XPS data were obtained on a Kratos Axis Ultra DLD system using a fixed anode monochromatic Al K_α X-ray source operating at 120 W. TGA data were collected on a Setaram Setsys Evolution TGA instrument. The sample was heated under Ar from 20 ^oC until 800 ^oC at 10 K per minute. SAXS data was taken on beamline I22 at Diamond, using a Pilatus P3-2M detector, with 12.4keV X-rays, and a 6 m sample to detector distance, which gave a Q range of 0.003-0.35 $Å^{-1}$. The powder samples were held between two pieces of Kapton tape. Data was reduced using the DAWN small angle scattering pipeline, calibrated against silver behenate to obtain Q, and the background scattering from the Kapton tape subtracted prior to analysis.

For BET measurements on a Quantachrome Autosorb-1, each sample was degassed under vacuum at 120°C until the no further degassing was observed (*ca* 24 h). Using nitrogen as the adsorbing gas at -196 ^oC (77 K), an 80 point physisorption analysis was undertaken and the data analysed by the DFT method. The model used was N_2 at 77 K on carbon (slit pore, NLDFT equilibrium model). Surface area of the samples was calculated using the BET method using a 5-point analysis.

2.3. Procedure for Film Carbonization

A solution of 1 mg cm^{-3} PIM-EA-TB in chloroform was prepared and then deposited onto the ITO electrode by drying under ambient conditions. Carbonization of the PIM-EA-TB powder or film was performed at 500 ^{o}C for 3 h under vacuum (Edwards oil pump) in a custom-made quartz tube to fit the furnace (TSH12, Elite Thermal Systems Ltd.).

3. Results and Discussion

3.1. cPIM Film Electrodes I.: Formation and Characterisation

The PIM-EA-TB material (referenced here as PIM) was obtained in powder form and dissolved in chloroform for casting of films on tin-doped indium oxide (ITO) coated glass substrates. Both powder and films were carbonised under vacuum at 500°C in a quartz tube and for 3 h. Figure 2A shows scanning electron micrographs with the morphology of the original PIM powder (white) exhibiting agglomerated particles typically 80-300 nm in diameter. After vacuum heat treatment at 500°C the carbonized PIM (cPIM) appears visually black, but has retained particle diameter and morphology (Figure 2B). Similarly, thin transparent and colourless PIM films cast on ITO (Figure 2C) are carbonised to give thin black hetero-carbon cPIM membranes (Figure 2D) with typically 1-2 μm thickness. Raman spectroscopy (532 nm excitation) reveals the associated structural changes, with PIM exhibiting an underlying fluorescence and characteristic peaks (Figure 2E), whereas cPIM samples show no fluorescence and typical broad peaks at 1380 cm^{-1} (D-peak, disordered amorphous carbon) and at 1600 cm^{-1} (G-peak, graphitic carbon)[36] (see Figure 2F). SAXS analysis of powder samples before and after carbonisation suggest the sample

contains features with a Guinier radius of gyration of 26 nm, in both cases (Figure 2G). If a spherical geometry is assumed, this corresponds to a feature radius around 34 nm.

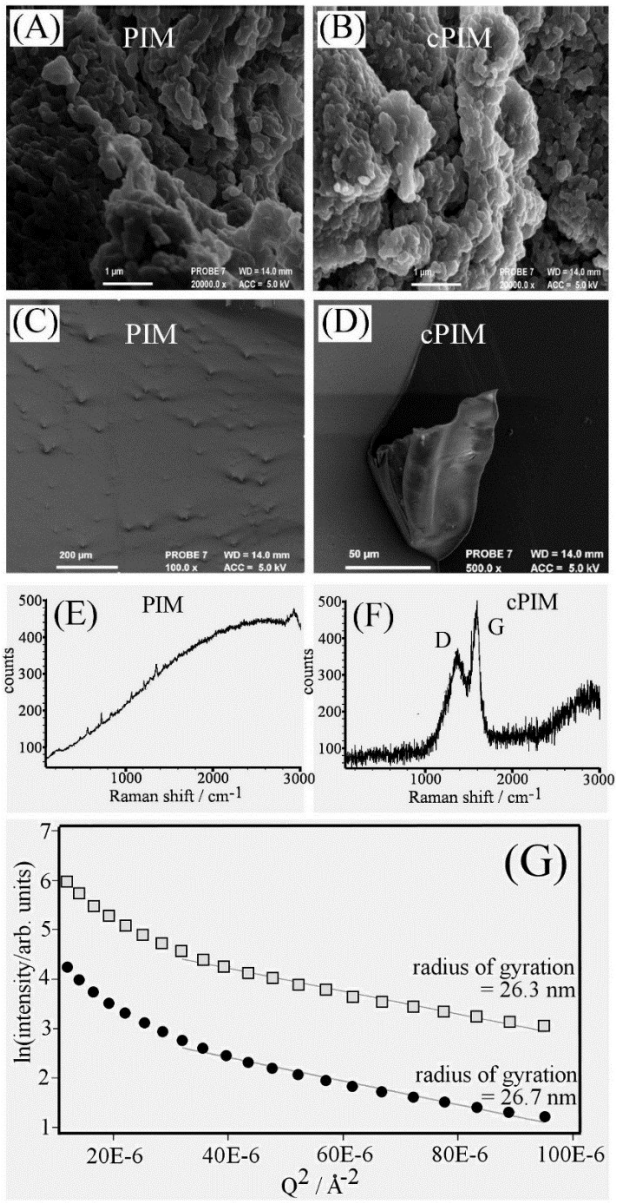

Figure 2. FESEM images of (A) PIM powder (B) cPIM powder after 3h carbonisation. (C) FESEM images of PIM film and (D) cPIM film on ITO after 3 h carbonisation. (E) Raman spectra for PIM powder and (F) for cPIM powder. (G) Guinier plots of the low angle region of the SAXS data for PIM and cPIM powder samples showing the region where the data was fitted to obtain the Guinier radii. The intensity at lowest angles was not used due to artefacts in the scattering close to the beamstop, which caused the plotted data to become non-linear. The data for the cPIM sample is offset for clarity.

In order to explore differences in electrical conductivity between PIM and cPIM materials, films were prepared on a glass slide (60 μg cm^{-2}). Four-point probe measurements reveal no evidence for electrical conductivity in the PIM film but Ohmic conductivity for the cPIM film (resistivity 40 MΩ/square). This value for a *ca*. 1-2 μm thick film is six orders of magnitude lower compared to the typical conductivity of the ITO layer and therefore consistent with relatively low electrical conductivity (*vide infra*).

Further insight into the elemental composition after carbonisation is obtained from XPS analysis (Figure 3). The survey scan for the PIM material reveals the presence of nitrogen (mainly 399 eV for sp^2-type nitrogen with a shoulder at 401 eV for protonated or alkylated nitrogen[37]) and of carbon (mainly 285 eV for C-C and C-H). In terms of atom% ratios the material shows C:N:O 91.9:6.56:1.54, consistent with 7 atom% nitrogen (in approximate agreement with the molecular structure in Figure 1).

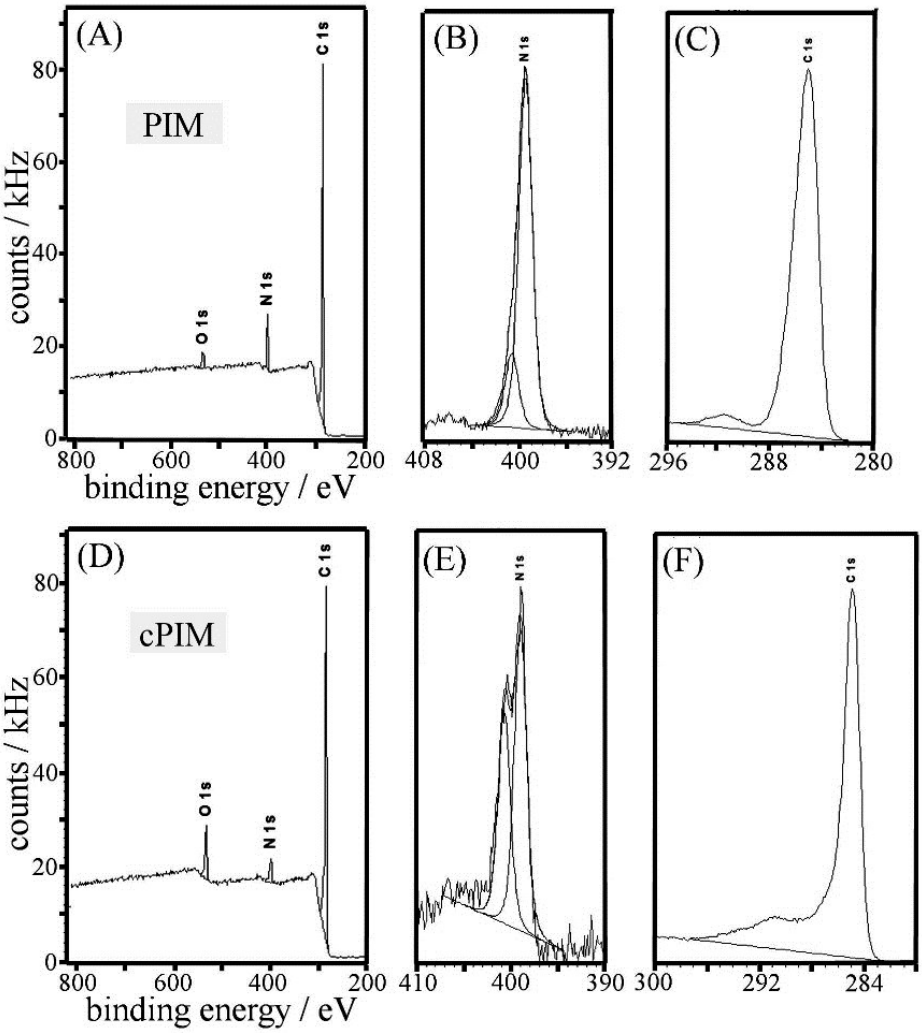

Figure 3. XPS survey data, the N1s region, and the C1s region respectively for PIM (A,B,C) and for cPIM (D,E,F).

After carbonisation the cPIM material shows oxygen, nitrogen, and carbon components in the survey XPS scan (Figure 3D). The carbon 1s signal not changed significantly (dominated by C-C/C-H), but the nitrogen signal now shows a clear split with more nitrogen being protonated or alkylated. The additional oxygen signal is likely to emerge from post-carbonisation reaction with air. The atom% ratio for C:N:O is now 89.8:4.44:5.76, which is indicative of only a minor loss of nitrogen, if any. The reaction

scheme in Figure 1 could be a realistic description of the cPIM molecular structure evolution. The BET adsorption isotherm and pore size analysis (see Figure 4) confirm the retention of the rigid backbone structure during carbonisation of PIM powder.

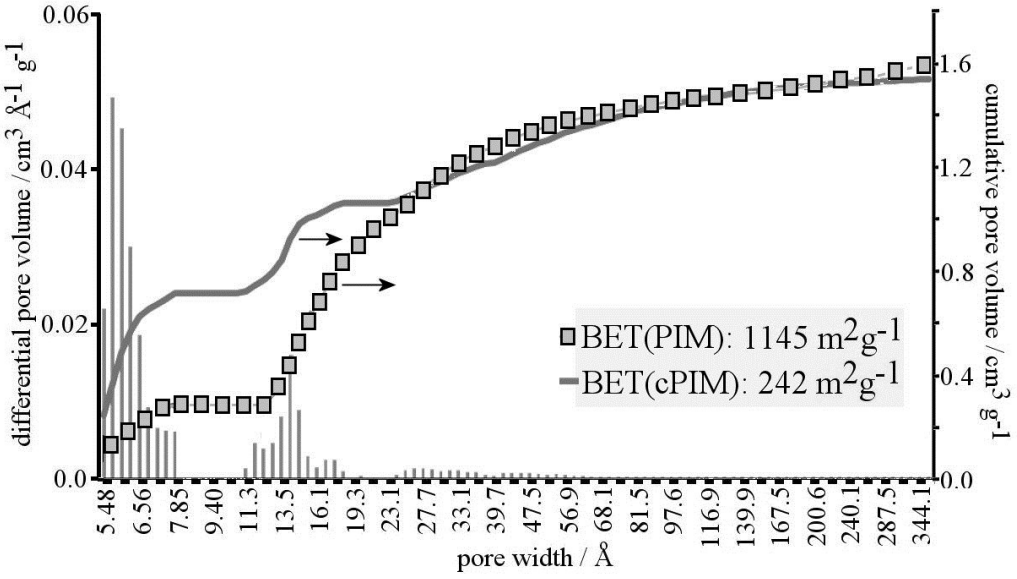

Figure 4. Plots of data from the 80-point BET pore size analysis for cPIM (N_2, 77K, slit pore NLDFT equilibrium model[38]) showing dominant pore sizes around 5.5 Å. A comparison of the cumulative pore volume for PIM (squares) and for cPIM (line) shows the switch from mesopores in PIM to micropores in cPIM.

The pore size analysis for cPIM powder shows a dominant pore size at *ca*. 5.5 Å or micropores responsible for half of the cumulative pore volume. A comparison to data for the PIM starting material (Figure 4) shows that the total cumulative pore volume has been retained (consistent with minimal morphology changes) but mesopores of *ca*. 14 Å size have been converted to the smaller micropores (due to crosslinking of polymer chains, see Figure 1). The BET area in cPIM is reduced to 242 m^2g^{-1}. This value seems average (or even low) when compared for example to novel graphene aerogel materials with up to an

order of magnitude higher BET surface area.[39] However, for cPIM the link from molecular precursor to 3D-carbon structure and the absence of any templating agents are novel and potentially useful for the design of materials, for further optimisation, or for the introduction of new functionalities.

3.2. cPIM Film Electrodes II.: Voltammetry and Capacitive Charging

Voltammetric characterisation of the cPIM film electrodes on ITO substrates was performed in aqueous buffer solution. In 0.1 M phosphate buffer pH 7 and in a potential range from 0.0 to 0.5 V vs. SCE a well-defined capacitance response is observed (Figure 5A). Initially, for 15 μg and 30 μg films (thickness *ca*. ¼ or ½ μm, respectively) the capacitance scales approximately linearly with the amount of cPIM deposited. However, for 60 μg and 120 μg the increase in capacitive current response ceases, consistent with an "active thickness" (or a resistive diffusion layer thickness due to diffusion of either electrons or ions or both) of less than 1 μm. For thicker films "charge diffusion" may require more time (*vide infra*). When exploring the effect of pH on the capacitive current, an interesting switch to considerably higher capacitance is observed at pH 2 (see Figure 5B). In fact, the onset of this increase in capacitance is seen already at pH 7 in the lower region of the potential window and the capacitance increase is shifted by *ca*. 0.35 V for a change in pH from 7 to 2. This Nernstian shift clearly proves the presence of a proton uptake reaction associated with the increase in capacitive current (e.g. protonation of nitrogen sites in cPIM associated with reduction). The effect can be compared to the step in capacitance in acidic solution observed for example in mesoporous hetero-carbon materials obtained from gelatin carbonisation with the help of a silica template.[40] This is a

feature uncommon to pure carbon materials and usually more associated with surface functionalities or with well-defined molecular structures.[41,42]

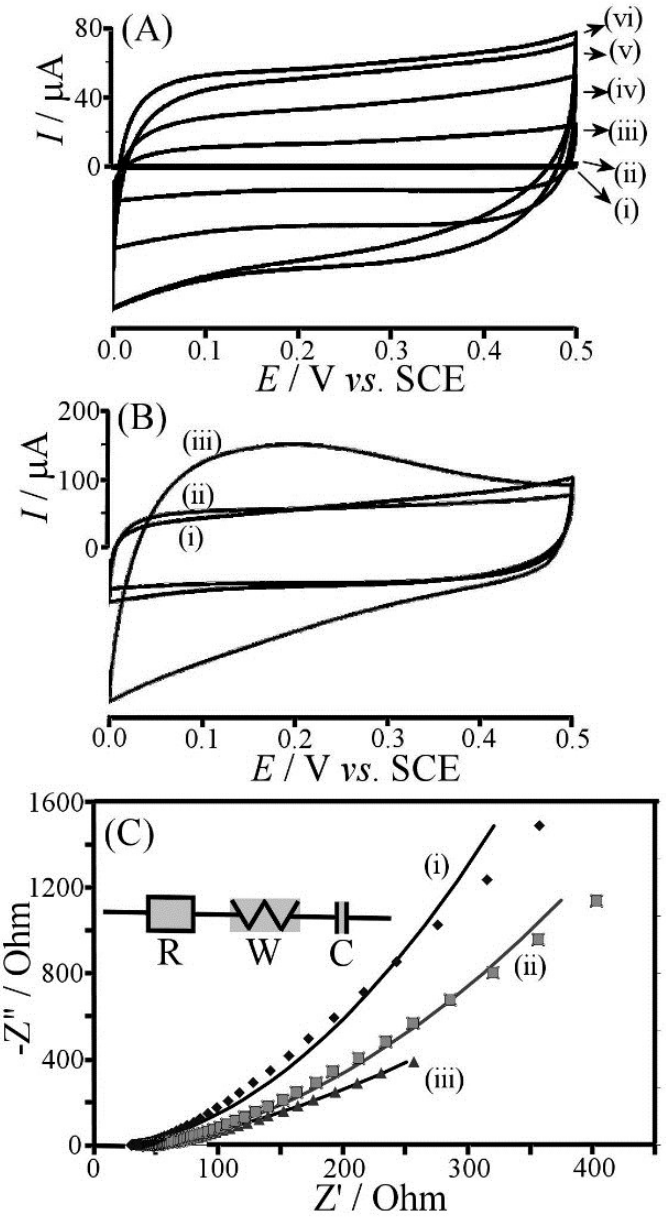

Figure 5. (A) Cyclic voltammograms (scan rate 50 mV s^{-1}) for different thicknesses of carbonized cPIM on ITO (with (i) bare ITO, (ii) 15 μg PIM, (iii) 15 μg cPIM, (iv) 30 μg cPIM, (v) 60 μg cPIM, and (vi) 120 μg cPIM) immersed in aqueous 0.1 M phosphate buffer pH 7. (B) As in A, but for 60 μg carbonized cPIM in 0.1 M phosphate buffer at (i) pH 12, (ii) pH 7, (iii) pH 2. (C) Nyquist plots for impedance data (0.0 V vs. SCE bias; 10 kHz to 0.1 Hz; 20 mV amplitude) for a 60 μg cPIM film immersed in 0.1 M phosphate buffer at (i) pH 12, (ii) pH 7, and (iii) pH 2.

Further study of the electrochemical impedance responses (Figure 5C) reveals characteristics consistent with those observed in cyclic voltammetry. A bare ITO electrode is observed to give a response consistent with an RC equivalent circuit (not shown) with R = 114 Ohm and C = 28 μF. The resistance R is dominated by the ITO sheet resistance, which is decreased during the vacuum heating process. After carbonisation, when investigating a 60 μg cPIM film on ITO different types of responses are recorded at pH 12, 7, and 2. All of these are approximately consistent with an RWC equivalent circuit (see Figure 5C) revealing some "charge diffusion" as well as a capacitive element dominating at very low frequencies (see Table 1). At pH 2 the capacitance can be extrapolated to 8.8 mF for 60 μg cPIM equivalent to an approximate "supercapacitance" of 146 Fg^{-1}. This estimated value is linked to the high microporosity of the material and the Faradaic current component with proton uptake and can be compared for example to typical graphene nano-ribbon materials[43] which exhibit typically 15 Fg^{-1}. Further improvements in "supercapacitance" and conductivity are likely to be achievable with further optimisation of the carbonisation process, although future application of the cPIM material are probably more likely in sensing or in mixed ion/electronic conductors.

Table 1. Summary of impedance data for cPIM film electrodes on ITO substrates immersed in 0.1 M phosphate buffer pH 2, 7, and 12.

	R / Ohm	W / Ohm	C / mF
Bare ITO	114	-	0.028
cPIM pH 2	44	164	8.8
cPIM pH 7	44	262	2.0
cPIM pH 12	27	232	1.3

When investigating the electrochemical properties of cPIM films over a wider potential window, additional features can be observed (Figure 6). With only PIM deposited (or a bare ITO) the reduction of ambient oxygen occurs with an onset at -0.2 V vs. SCE (Figure 6A). A much stronger oxygen reduction response is observed for a 15 μg cPIM film on ITO, but this can be traced back to the vacuum heat treatment activation of the underlying ITO substrate[44,45,46] (*vide infra*). The resulting reduction current of ca. 40 μA is consistent with ambient oxygen at the ITO substrate. When increasing the cPIM layer thickness (see Figure 6C) the capacitive current response increases, but the Faradaic current for oxygen reduction remains. Additional experiments were conducted with hydrogen peroxide, H_2O_2 (Figure 6D-F). The current for the reduction of H_2O_2 is observed at bare or PIM-coated ITO as well as at the cPIM-coated ITO. The current response is not diffusion controlled

and therefore incomplete reduction occurs in this potential range. Comparison of data with/without cPIM film suggests again that the carbonised polymer is not reactive and that the underlying ITO substrate is where the reduction occurs instead.

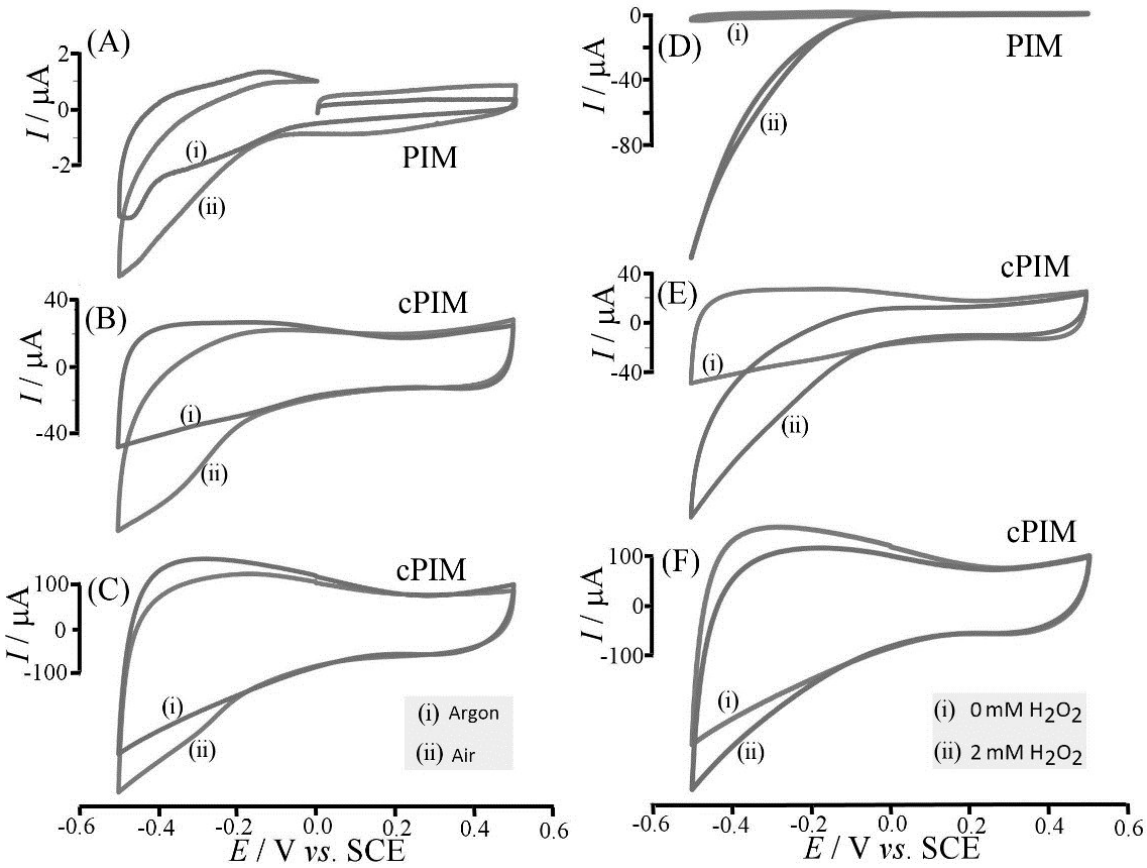

Figure 6. (A,B,C) Cyclic voltammograms (scan rate 50 mVs^{-1}; (A) 15 µg PIM on ITO; (B) 15 µg cPIM on ITO; (C) 60 µg cPIM on ITO) in 0.1 M phosphate buffer pH 7 (i) in the absence and (ii) in the presence of air/oxygen. (D,E,F) as above, but for (i) 0 mM and (ii) 2 mM H_2O_2.

3.3. cPIM Film Electrodes III.: Oxygen Reduction and Scanning Electrochemical Microscopy

It appears that the cPIM material, although exhibiting an extremely high surface area and electrochemical reduction with insertion of protons, is not able to directly transfer electrons to oxygen or to hydrogen peroxide. This effect can be further demonstrated by scanning electrochemical microscopy (SECM[47,48]) in the generator-collector mode, employing a platinum microelectrode tip to measure the formation of hydrogen peroxide during oxygen reduction (Figure 7). The currents observed at bare ITO or cPIM-coated ITO in non-deaerated phosphate buffer solution appear very similar in the second and following potential cycles (In the first potential cycle cPIM-coated ITO exhibits a stronger signal possibly due to some oxygen adsorption, see Figure 7Bi). However, the corresponding tip current signals (proportional to H_2O_2 concentration over the sample surface) reveal a lower signal in the presence of the cPIM film as well as a hysteresis/lag in the maximum H_2O_2 current. Therefore the oxygen reduction at the underlying ITO substrate does produce some hydrogen peroxide that is released more slowly through the cPIM film with a delay induced by slow diffusion through the film of porous carbon. This result confirms the very slow rate of electron transfer for both molecular oxygen and H_2O_2 in contact with microporous cPIM under reducing conditions. This effect is most likely due to the absence of reactive sites for electron transfer in cPIM. The unusual current "crossing" of the current over bare ITO (line (i) in Figure 7C is likely to be associated with a surface reactivity change at the ITO electrode when scanning the potential more negative.

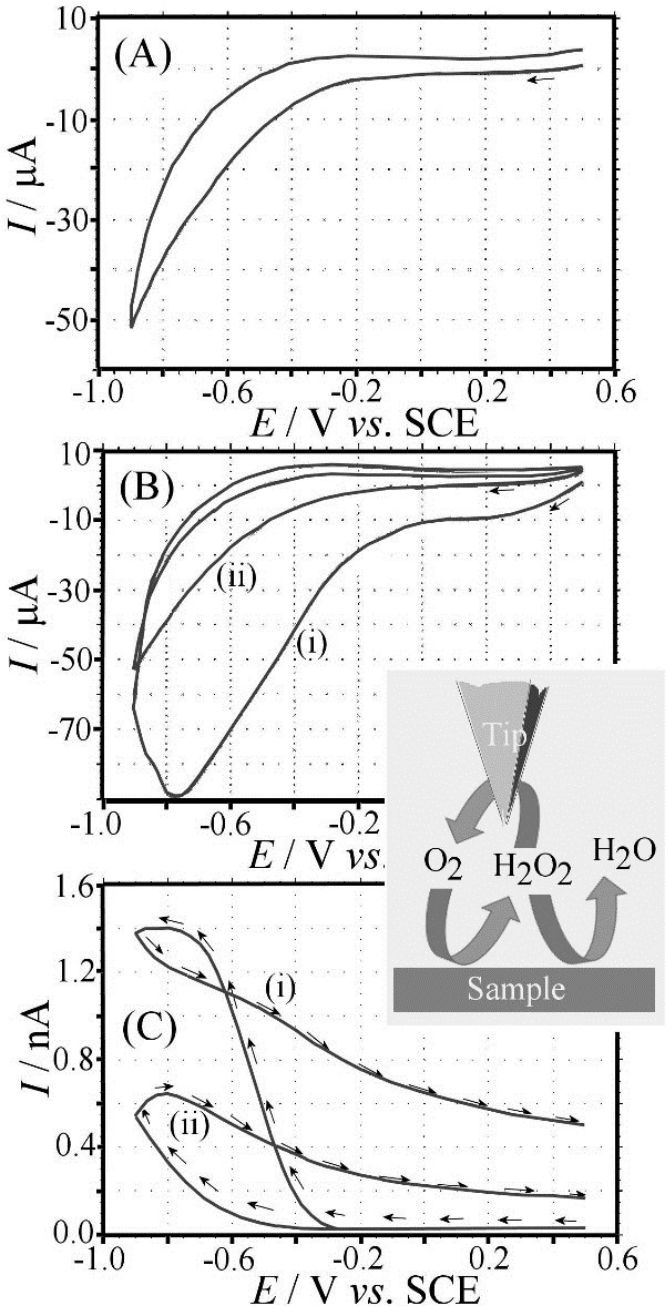

Figure 7. Scanning electrochemical microscopy (SECM, scan rate 50 mVs^{-1}, tip potential 0.6 V vs. SCE, tip distance ca. 5 μm) data for (A) a heat-treated ITO electrode in 0.1 M phosphate buffer pH 7, (B) a 60 μg cPIM coated ITO electrode (1st (i) and 2nd (ii) potential cycle shown), and (C) the corresponding tip current for (i) bare ITO and (ii) cPIM coated ITO. Inset shows schematic drawing of the detection principle.

4. Conclusion

It is intriguing to find a high surface area hetero-carbon with a very high level of microporosity and "supercapacitive" charging, but without significant electron transfer reactivity towards oxygen or towards hydrogen peroxide. This combination of properties could be beneficial due to the destructive effects of the oxygen reduction reaction (and the resulting reactive oxygen species) on carbon electrode materials. Such behaviour may lead to suppressed carbon corrosion, for example for energy/charge storage devices operating in the presence of ambient oxygen.

More generally, it has been shown that the rigid polymer of intrinsic microporosity (PIM-EA-TB) can be carbonised under mild conditions without loss of morphology and with a switch from meso- to enhanced micro-porosity. The ability of this new material to undergo redox-driven proton insertion/expulsion (like a molecular conducting polymer[49]) whilst exhibiting capacitive charging (more like a carbon[50]) is of interest and could have important potential applications in sensing (for example in Chem-FETs[51]). Further work will be required for this new class of carbonised PIM materials, in particular to investigate the effects of charge diffusion rates, carbonisation temperature, molecular precursor structure, and dimensionality on the properties of the resulting microporous hetero-carbons. The potential for combined electron/ion conductivity needs to be investigated, for example to develop effective conductors for lithium-ion battery composites. New classes of designer carbons combining conductivity, microporosity, and hetero-atoms or functional groups could be beneficial in selective adsorbents or in electrochemical desalination processes.

Acknowledgement

Y.R. thanks the University of Bath for a fee waiver and the China Scholarship Council for a PhD stipend. We thank Dr Nick Terrill for assistance with the SAXS experiments and Diamond Light Source for access to beamline I22 (SM 11392-1) that contributed to the results presented here. A.J.W thanks the UK National Measurement System for financial support.

References

1. Sakaushi, K.; Antonietti, M. Carbon- and Nitrogen-Based Porous Solids: A Recently Emerging Class of Materials. *Bull. Chem. Soc. Japan* **2015**, *88*, 386-398.
2. Antonietti, M.; Fechler, N.; Fellinger, T.P. Carbon Aerogels and Monoliths: Control of Porosity and Nanoarchitecture via Sol-Gel Routes. *Chem. Mater.* **2014**, *26*, 196-210.
3. Lux, L.; Williams, K.; Ma, S.Q. Heat-Treatment of Metal-Organic Frameworks for Green Energy Applications. *CrystEngComm* **2015**, *17*, 10-22.
4. Zhang, S.G.; Dokko, K.; Watanabe, M. Carbon Materialization of Ionic Liquids: from Solvents to Materials. *Mater. Horizons* **2015**, *2*, 168-197.
5. Nishihara, H.; Kyotani, T. Templated Nanocarbons for Energy Storage. *Adv. Mater*. **2012**, *24*, 4473-4498.

6. Dutta, S.; Bhaumik, A.; Wu, K.C.W. Hierarchically Porous Carbon Derived from Polymers and Biomass: Effect of Interconnected Pores on Energy Applications. *Energy Environ. Sci.* **2014**, *7*, 3574-3592.
7. Vuorema, A.; Sillanpää, M.; Rassaei, L.; Wasbrough, M.J.; Edler, K.J.; Thielemans, W.; Dale, S.E.C.; Bending, S.; Wolverson, D.; Marken, F. Ultrathin Carbon Film Electrodes from Vacuum-Carbonised Cellulose Nanofibril Composite. *Electroanalysis* **2010**, *22*, 619-624.
8. Zhao, S.; Wang, C.Y.; Chen, M.M.; Wang, J.; Shi, Z.Q. Potato Starch-based Activated Carbon Spheres as Electrode Material for Electrochemical Capacitor. *J. Phys. Chem. Solids* **2009**, *70*, 1256-1260.
9. Shuttleworth, P.S.; Budarin, V.; White, R.J.; Gun'ko, V.M.; Luque, R.; Clark, J.H. Molecular-Level Understanding of the Carbonisation of Polysaccharides. *Chem. European J.* **2013**, *19*, 9351-9357.
10. Xia, F.J.; Pan, M.; Mu, S.C.; Jones, M.D.; Wolverson, D.; Marken, F. Chitosan-Based Hydrothermal Nanocarbon: Core-Shell Characteristics and Composite Electrodes. *Electroanalysis*, **2012**, *24*, 1703-1708.
11. Sun, G.L.; Li, B.; Ran, J.B.; Shen, X.Y.; Tong, H. Three-Dimensional Hierarchical Porous Carbon/Graphene Composites Derived from Graphene Oxide-Chitosan Hydrogels for High Performance Supercapacitors. *Electrochim. Acta* **2015**, *171*, 13-22.
12. Yang, D.S.; Chaudhari, S.; Rajesh, K.P.; Yu, J.S. Preparation of Nitrogen-Doped Porous Carbon Nanofibers and the Effect of Porosity, Electrical Conductivity, and Nitrogen Content on Their Oxygen Reduction Performance. *ChemCatChem* **2014**, *6*, 1236-1244.
13. Ahn, S.D.; Mao, B.Y.; Pascu, S.I.; Vuorema, A.; Mitchels, J.M.; Marken, F. Ion-Transfer Voltammetry at Carbon Nanofibre Membranes Produced by 500 Degrees C Graphitisation/Graphenisation of Electrospun Poly-Acrylonitrile. *Electroanalysis* **2014**, *26*, 69-75.
14. Lawrence, K.; Xia, F.J.; Arrowsmith, R.L.; Ge, H.B.; Nelson, G.W.; Foord, J.S.; Felipe-Sotelo, M.; Evans, N.D.M.; Mitchels, J.M.; Flower, S.E.; Botchway, S.W.; Wolverson, D.; Aliev, G.N.; James, T.D.; Pascu, S.I.; Marken, F. Hydrothermal

Conversion of One-Photon-Fluorescent Poly(4-vinylpyridine) into Two-Photon-Fluorescent Carbon Nanodots. *Langmuir* **2014**, *30*, 11746-11752.

15. Liu, L.; Liao, L.H.; Meng, Q.H.; Cao, B. High Performance Graphene Composite Microsphere Electrodes for Capacitive Deionisation. *Carbon* **2015**, *90*, 75-84.
16. Yan, J.; Wang, Q.; Wei, T.; Jiang, L.L.; Zhang, M.L.; Jing, X.Y.; Fan, Z.J. Template-Assisted Low Temperature Synthesis of Functionalized Graphene for Ultrahigh Volumetric Performance Supercapacitors. *ACS Nano* **2014**, *8*, 4720-4729.
17. Bazargan, A.; Hui, C.W.; McKay, G. Porous Carbons from Plastic Waste. Long, T.E.; Voit, B.; Okay, O. (ed.) *Porous Carbons - Hyperbranched Polymers Polymer Solvation* **2015**, Book Series: Advances in Polymer Science, *266*, 1-25.
18. Qian, K.Z.; Kumar, A.; Zhang, H.L.; Bellmer, D.; Huhnke, R. Recent Advances in Utilization of Biochar. *Renew. Sust. Energy Rev.* **2015**, *42*, 1055-1064.
19. Ramos, A.; Camean, I.; Garcia, A.B. Graphitization Thermal Treatment of Carbon Nanofibers. *Carbon* **2013**, *59*, 2-32.
20. Tang, J.; Liu, J.; Torad, N.L.; Kimura, T.; Yamauchi, Y. Tailored Design of Functional Nanoporous Carbon Materials Toward Fuel Cell Applications. *Nano Today* **2014**, *9*, 305-323.
21. Harikrishnan, G.; Patro, T.U.; Khakhar, D.V., Reticulated Vitreous Carbon From Polyurethane Foam-Clay Composites. *Carbon* **2007**, *45*, 531-535.
22. Hao, L.; Liu, X.L.; Wang, J.T.; Wang, C.; Wu, Q.H.; Wang, Z. Use of ZIF-8-Derived Nanoporous Carbon as the Adsorbent for the Solid Phase Extraction of Carbamate Pesticides Prior to High-Performance Liquid Chromatographic Analysis. *Talanta* **2015**, *142*, 104-109.
23. Gadipelli, S.; Guo, Z.X. Tuning of ZIF-Derived Carbon with High Activity, Nitrogen Functionality, and Yield - A Case for Superior CO_2 Capture. ChemSusChem 2015, 8, 2123-2132.
24. Aijaz, A.; Fujiwara, N.; Xu, Q. From Metal-Organic Framework to Nitrogen-Decorated Nanoporous Carbons: High CO_2 Uptake and Efficient Catalytic Oxygen Reduction. *J. Amer. Chem. Soc.* **2014**, *136*, 6790-6793.

25. Amali, A.J.; Sun, J.K.; Xu, Q. From Assembled Metal-Organic Framework Nanoparticles to Hierarchically Porous Carbon for Electrochemical Energy Storage. *Chem. Commun.* **2014**, *50*, 1519-1522.

26. Gadipelli, S.; Guo, Z.X. Tuning of ZIF-Derived Carbon with High Activity, Nitrogen Functionality, and Yield - A Case for Superior CO_2 Capture. *ChemSusChem*, **2015**, *8*, 2123-2132.

27. Li, Z.Q.; Yin, L.W. MOF-derived, N-doped, Hierarchically Porous Carbon Sponges as Immobilizers to Confine Selenium as Cathodes for Li-Se Batteries with Superior Storage Capacity and Perfect Cycling Stability. *Nanoscale*, **2015**, *7*, 9597-9606.

28. McKeown, N.B.; Budd, P.M. Polymers of Intrinsic Microporosity (PIMs): Organic Materials for Membrane Separations, Heterogeneous Catalysis and Hydrogen Storage. *Chem. Soc. Rev.* **2006**, *35*, 675-683.

29. Carta, M.; Bernardo, P.; Clarizia, G.; Jansen, J.C.; McKeown, N.B. Gas Permeability of Hexaphenylbenzene Based Polymers of Intrinsic Microporosity. *Macromolecules* **2014**, *47*, 8320-8327.

30. Kim, S.; Lee, Y.M. Rigid and Microporous Polymers for Gas Separation Membranes. *Prog. Polymer Sci.* **2015**, *43*, 1-32.

31. Baker, R.W.; Low, B.T. Gas Separation Membrane Materials: A Perspective. *Macromolecules*, **2014**, *47*, 6999-7013.

32. Wang, Y.; McKeown, N.B.; Msayib, K.J.; Turnbull, G.A.; Samuel, I.D.W. Laser Chemosensor with Rapid Responsivity and Inherent Memory Based on a Polymer of Intrinsic Microporosity. *Sensors* **2011**, *11*, 2478-2487.

33. Xia, F.J.; Pan, M.; Mu, S.C.; Malpass-Evans, R.; Carta, M.; McKeown, N.B.; Attard, G.A.; Brew, A.; Morgan, D.J.; Marken, F. Polymers of Intrinsic Microporosity in Electrocatalysis: Novel Pore Rigidity Effects and Lamella Palladium Growth. *Electrochim. Acta* **2014**, *128*, 3-9.

34. Madrid, E.; Cottis, P.; Rong, Y.Y.; Rogers, A.T.; Stone, J.M.; Malpass-Evans, R.; Carta, M.; McKeown N.B.; Marken F. Water Desalination Concept Using an Ionic Rectifier Based on a Polymer of Intrinsic Microporosity (PIM). *J. Mater. Chem. A* **2015**, DOI: 10.1039/C5TA04092B.

35. Carta, M.; Malpass-Evans, R.; Croad, M.; Rogan, Y.; Jansen, J.C.; Bernardo, P.; Bazzarelli, F.; McKeown, N.B. An Efficient Polymer Molecular Sieve for Membrane Gas Separations. *Science* **2013**, *339*, 303-307.

36. Ferrari, A.C. Raman Spectroscopy of Graphene and Graphite: Disorder, Electron-Phonon Coupling, Doping and Nonadiabatic Effects. *Solid State Commun*. **2007**, *143*, 47-57.

37. Shibata, M.; Kimura, Y.; Yaginuma, D. Thermal Properties of Novel Supramolecular Polymer Networks Based on Poly(4-vinylpyridine) and Disulfonic Acids. *Polymer*, **2004**, *45*, 7571-7577.

38. Ghanem, B.S.; Swaidan, R.; Litwiller, E.; Pinnau, I. Ultra-Microporous Triptycene-based Polyimide Membranes for High-Performance Gas Separation. *Adv. Mater*. **2014**, *26*, 3688-3692.

39. Wang, H.; Yuan, X.Z.; Zeng, G.M.; Wu, Y.; Liu, Y.; Jiang, Q.; Gu, S.S., Three dimensional graphene based materials: Synthesis and applications from energy storage and conversion to electrochemical sensor and environmental remediation. *Adv. Coll. Interfac. Sci*. **2015**, *221*, 41-59.

40. Olejniczak, A.; Lezanska, M.; Pacula, A.; Nowak, P.; Wloch, J.; Lukaszewicz, J.P., Nitrogen-containing mesoporous carbons with high capacitive properties derived from a gelatin biomolecule. *Carbon* **2015**, *91*, 200-214.

41. Lin, P.; Yan, F. Organic Thin-Film Transistors for Chemical and Biological Sensing. *Adv. Mater.* **2012**, *24*, 34-51.

42. Janosevic, A.; Marjanovic, B.; Rakic, A.; Ciric-Marjanovic, G. Progress in Conducting/Semiconducting and Redox-Active Oligomers and Polymers of Arylamines. *J. Serb. Chem. Soc.* **2013**, *78*, 1809-1836.

43. Goh, M.S.; Pumera, M. Multilayer graphene nanoribbons exhibit larger capacitance than their few-layer and single-layer graphene counterparts. *Electrochem. Commun*. **2010**, *12*, 1375-1377.

44. Latz, R.; Michael, K.; Scherer, M. High Conducting Large Area Indium Tin Oxide Electrodes for Displays Prepared by DC Magnetron Sputtering. *Japan. J. Appl. Phys. 2-Lett*. **1991**, *30*, L149-L151.

45. Vacca, P.; Petrosino, M.; Chierchia, R.; Guerra, A.; Minarini, C.; Rubino, A. Influence of Electrical, Chemical and Morphological Properties of Inorganic/Organic Interface on Light Emitting Devices Performance. *Macromol. Symposia* **2007**, *247*, 333-339.

46. Collins, A.M.; Blanchard, G.J.; Marken, F. Spectroelectrochemical Investigation of TPPMn(III/II)-Driven Liquid | Liquid | Electrode Triple Phase Boundary Anion Transfer into 4-(3-Phenylpropyl)-Pyridine: ClO_4^-, CO_3H^-, Cl^-, and F^-. *Electroanalysis*, **2012**, *24*, 246-253.

47. Amemiya, S.; Bard, A.J.; Fan, F.R.F.; Mirkin, M.V.; Unwin, P.R. Scanning Electrochemical Microscopy. *Annual Rev. Anal. Chem.*, **2008**, *1*, 95-131.

48. Nagy, G.; Nagy, L. Scanning Electrochemical Microscopy: a New Way of Making Electrochemical Experiments. *Fresenius J. Anal. Chem.* **2000**, *366*, 735-744.

49. Li, C.; Bai, H.; Shi, G.Q. Conducting Polymer Nanomaterials: Electrosynthesis and Applications. *Chem. Soc. Rev.* **2009**, *38*, 2397-2409.

50. Gross, A.J.; Downard, A.J. Regeneration of Pyrolyzed Photoresist Film by Heat Treatment. *Anal. Chem.* **2011**, *83*, 2397-2402.

51. Vonau, W.; Guth, U. PH Monitoring: a Review. *J. Solid State Electrochem.* **2006**, *10*, 746-752.

TOC graphic entry: